Materials Science & Engineering A 670 (2016) 75–80

Contents lists available at ScienceDirect

Materials Science & Engineering A

journal homepage: www.elsevier.com/locate/msea

Study of spark plasma sintered nanostructured ferritic steel alloy with silicon carbide addition

Zhihao Hu, Kaijie Ning, Kathy Lu *

Department of Materials Science and Engineering, Virginia Polytechnic Institute and State University, Blacksburg, VA 24061, USA

ARTICLE INFO

Article history:
Received 13 April 2016
Received in revised form
31 May 2016
Accepted 1 June 2016
Available online 3 June 2016

Keywords:
Nanostructured ferritic alloy (NFA)
Silicon carbide (SiC)
Spark plasma sintering (SPS)
Density
Microstructure
Hardness

ABSTRACT

Pure nanostructured ferritic steel alloy (NFA) and NFA–silicon carbide (SiC) composites with different compositions (97.5 vol% NFA-2.5 vol% SiC and 95 vol% NFA-5 vol% SiC) have been sintered by spark plasma sintering (SPS) and systematically investigated based on XRD, SEM, density, Vickers hardness, and nano-hardness. Minor γ-Fe phase formation from the main α-Fe matrix occurs in pure NFA between the sintering temperature of 950 °C and 1000 °C. However, this is hindered in the NFA-SiC composite sintering. Densities for both the pure NFA and the NFA-SiC composites increase with the sintering temperature but decrease with the SiC content. The NFA-SiC composites have higher porosity than pure NFA under the same sintering condition. All the samples have the average grain sizes between 6 μm and 8 μm. Vickers hardness of the pure NFA and NFA-SiC composites is related to density and phase composition. By estimation, the 97.5 vol% NFA-2.5 vol% SiC composite sample has the maximum yield strength of 3.14 ± 0.18 GPa. Nano-hardness of the NFA-SiC composite is degraded by diffusion and reaction between NFA and SiC. The addition of SiC decreases the elastic modulus of the NFA-SiC composites.

1. Introduction

Cladding materials for nuclear fission and fusion energy systems are exposed to very high doses of neutron irradiation at high temperatures. These materials are required to maintain mechanical integrity over long term operation under such harsh environments [1–3]. Due to the excellent creep and irradiation resistances, nanostructured ferritic alloy (NFA) materials have been considered as a primary candidate for fission and fusion reactors [4]. The enriched nanoclusters and nanograined Fe-Cr alloy matrix of NFA materials [5–7] can enable mechanical enhancement and radiation resistance, for which traditional oxide dispersion strengthened (ODS) alloys are not able to achieve. The nanoclusters in the NFA alloys not only play the critical role of preventing dislocation gliding, grain growth, grain boundary slip, but also function as sinks to trap helium atoms and radiation-generated point defects. In addition, NFAs have excellent creep resistance, high temperature strength, and highly delayed radiation effects due to the prominent thermal stability of nanoclusters [4,7–11]. As a result, NFAs are desirable radiation shielding materials.

Silicon carbide (SiC) [12] is another structural material with high strength and chemical stability, especially in harsh environments. Even when exposed to radiation for a long time, SiC materials [13–15] still have low induced activation and low afterheat levels. SiC fiber-reinforced SiC-matrix composites (SiC_f/SiC) have prominent structural applications due to the enhanced mechanical properties and damage tolerance [16]. They are being considered as promising candidates for fuel cladding and channel boxes in light water reactors (LWR) and in-vessel components for advanced fission reactors [17–19].

Composite materials of NFA-SiC are expected to combine these advantages from each component. Such a composite would not only take advantage of the plastic deformation and energy absorption from the ductile NFA phase, but also provide the crack-propagation impedance for the highly brittle SiC. Meanwhile, the SiC component in the NFA-SiC composite would enhance high temperature stability that pure metallic structural materials cannot withstand and tolerate chemically harsh environments. As a result, the addition of SiC should reinforce the NFA matrix while the resistance to radiation is maintained.

In order to achieve high density for the NFA-SiC composites, spark plasma sintering (SPS) was used in this study. The SPS process relies on a pulsed direct current (DC) passing through an electrically conducting pressure die containing the green sample to densify the samples [20–23]. Full density can be reached relatively easily, and the entire process only takes a few minutes, thus minimizing the grain growth and any potential reactions.

In this work, density and microstructure evolution at different sintering temperatures were studied. The effects of a small amount of SiC addition on the sintering of the SiC-NFA composites were

* Corresponding author.
E-mail address: klu@vt.edu (K. Lu).

http://dx.doi.org/10.1016/j.msea.2016.06.003
0921-5093/

analyzed. Mechanical properties, such as Vickers hardness, nano-hardness, yield strength, and elastic modulus of the sintered samples, were investigated, and yield strength was derived from the hardness data.

2. Experimental procedures

2.1. Sample preparation and sintering

Commercial SiC particles (Grade UF-15, α-SiC, H.C. Starck, Karlsruhe, Germany) and lab-made NFA particles [4,7] were used as raw materials for pure NFA and NFA-SiC composite sintering. The NFA particles were screened with a mesh size of No. 653 (20 μm). Mean particle sizes for SiC and NFA were measured using a laser light scattering particle size analyzer (LA-950, HORIBA Scientific, Tenyamachi, Japan). The corresponding sizes were 1.24 μm and 14.28 μm, respectively. Ball-milling for the NFA and SiC powders was conducted in order to achieve homogeneous mixing. Then the powders were poured into a cylinder die, which had 20 mm diameter. The powder height was controlled at 5 mm. The densification process of the pure NFA and NFA-SiC composites was performed by spark plasma sintering (SPS Nanoceramics, Morton Grove, IL). Main sintering parameters included pressure (100 MPa), heating rate (50 °C/min), temperature (850 °C, 900 °C, 950 °C, 1000 °C), and holding time (10 min) for the pure NFA, 97.5 vol% NFA-2.5 vol% SiC, and 95 vol% NFA-5 vol% SiC samples.

2.2. Characterization

The density of the sintered samples was measured based on the Archimedes method. The phase composition was identified by X-ray diffraction (XRD, PANalytical B.V., Almelo, Netherlands). The microstructure was observed by scanning electron microscopy (FEI FEG-ESEM Quanta600, FEI Company, Hillsboro, OR, USA). Before the SEM observation, the sample surfaces were finely polished and ultrasonically cleaned. The elemental composition was measured by the energy-dispersive X-ray spectroscopy module (EDS, Bruker AXS, MiKroanalysis B.V., Gmbh, Berlin, Germany) attached to the SEM. The average grain sizes were measured from the ethanol-nitric acid etched surface. The statistical estimation for the average grain size was conducted for each sample with the grain number no less than 150. Vickers hardness was measured by using a macro-hardness tester (LV700AT, LECO, St. Joseph, MI). Fifteen indentations were performed for each sample with a load of 3 kg.

The Vickers hardness was calculated using the following formula [24,25]:

$$H_V = k\left(\frac{P}{d^2}\right) \quad (1)$$

where k is the shape factor of the indenter, P is the load to the indenter, d is the diagonal length of the indention.

The yield strength was calculated using the following formula [26–28]:

$$\sigma_{YS} = \frac{1}{3}H_v \quad (2)$$

where σ_{YS} is the yield strength, which has the unit of GPa.

The nano-hardness was measured by nano-indentation (TI 950 Triboindenter, Hysitron, Inc., Minneapolis, MN). A 100 nm 3-sided pyramidal diamond Berkovich tip was used during the measurement. A nano-indentation array of 15 indents was performed for each sample. The peak load was kept at 4000 μN for all the nano-indents. All the above measurements were conducted at room temperature.

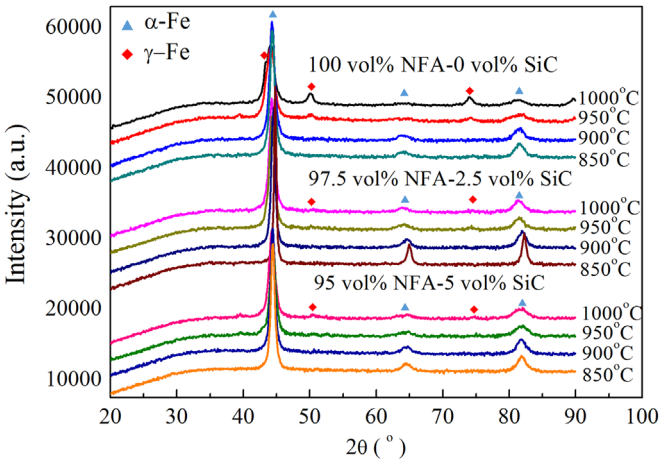

Fig. 1. XRD patterns of sintered pure NFA and NFA-SiC composite samples with different temperatures.

3. Results and discussion

3.1. Phase analysis

Fig. 1 shows the XRD patterns of the pure NFA, 97.5 vol% NFA-2.5 vol% SiC, and 95 vol% NFA-5 vol% SiC samples at different sintering conditions. All the samples show the well-crystallized α-Fe XRD patterns, and no SiC peaks can be observed. There are new peaks from γ-Fe at 950 °C and 1000 °C, while there are only peaks from α-Fe at 850 °C and 900 °C. This is because the onset temperature of the α→γ Fe phase transformation is 948 °C [29]. In addition, the 100 vol% NFA sample after 1000 °C sintering gives the most obvious peaks from γ-Fe, while the 95 vol% NFA-5 vol% SiC and 97.5 vol% NFA-2.5 vol% SiC samples have only very small peaks from γ-Fe. This means that the addition of SiC delays the Fe $\alpha \rightarrow \gamma$ phase transformation and increases the phase transformation temperature.

Based on the Si-Fe phase diagram [30], when the atomic percent of Si is less than 3.8 at%, the phase transformation temperature increases with the increasing content of Si. In our system, the 95 vol% NFA-5 vol% SiC sample has 3.3 at% of Si. As a result, the phase transformation temperature increases from the 2.5 vol% SiC addition sample to the 5 vol% SiC addition sample. The fundamental process can be understood as follows. When sintering NFA-SiC composites, decomposition occurs and leads to the form of silicon and carbon at high temperatures [31–33]. It has been shown that the decomposition of SiC starts at 610 °C, then silicon diffuses into the lattice of iron to alloy with iron. The diffusion of silicon tends to de-stabilize γ-Fe and hinder the phase transformation of α-Fe→γ-Fe, raising the phase transformation temperature [34]. When the atomic percent of Si is above 3.8 at%, there is no phase transformation from α-Fe to γ-Fe. Thus, the composites with SiC addition tend to have a much smaller content of γ-Fe. This explains why γ-Fe phase could hardly be observed in the 95 vol% NFA-5 vol% SiC composite sample even with sintering at 1000 °C.

3.2. Microstructure

Fig. 2 shows the SEM images of the sintered pure NFA and NFA-SiC composite samples. In Fig. 2(a–d), the microstructures of the pure NFA samples show that the sintered bodies are fairly dense without obvious pores. The NFA-SiC samples in Fig. 2(e–h) and Fig. 2(i–l), however, show different levels of porosity. The 97.5 vol% NFA-2.5 vol% SiC samples and 95 vol% NFA-5 vol% SiC samples have similar change tendencies in pore shape and porosity with the sintering temperature. For both of them, pores tend to become

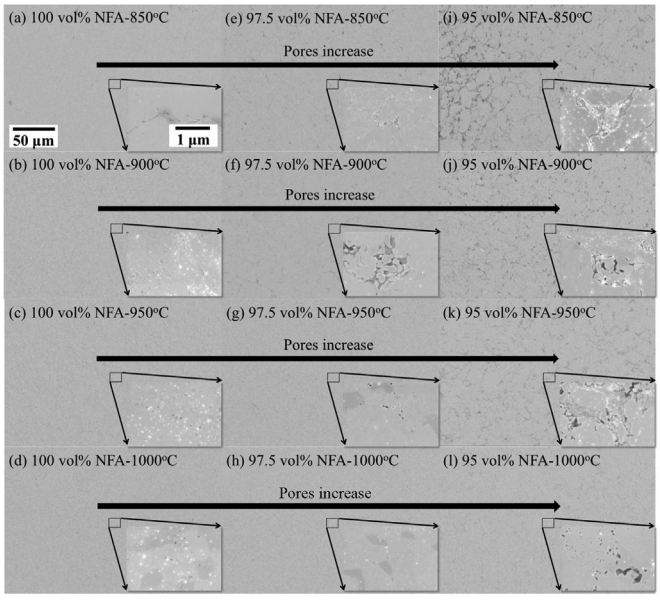

Fig. 2. SEM images of pure NFA and NFA-SiC composite samples with different sintering temperatures.

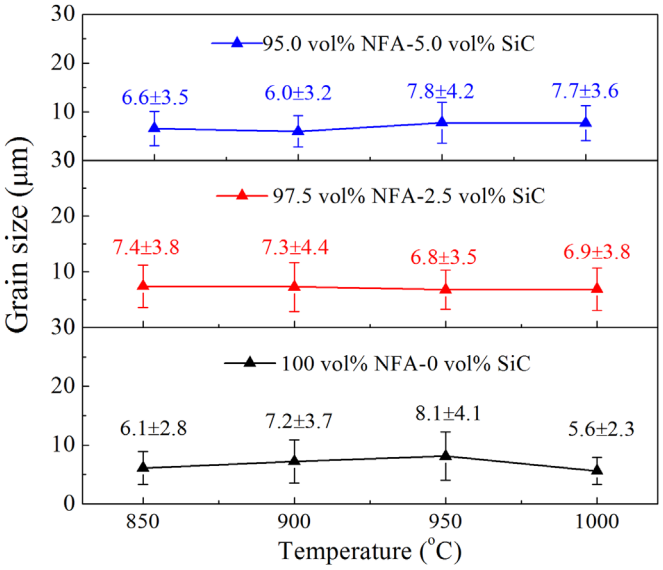

Fig. 3. Average grain sizes for pure NFA and NFA-SiC samples with different sintering temperatures.

closed and roundish and the pore amount gradually decreases with the increase of the sintering temperature. The major difference is that the latter samples have more pores at the same sintering temperature. It is believed that these pores are mainly from the reaction of NFA and SiC, which will be further discussed in Section 3.4. The bright phases from all the images shown in Fig. 2 are believed to the dispersed oxide nanoclusters from the NFA. The gray phase shown in Fig. 2(d) is probably γ-Fe precipitated from α-Fe at 1000 °C, while the gray phase shown near pores in Fig. 2(g–h) is considered to be the reaction products between NFA and SiC.

Fig. 3 shows the average grain sizes for the pure NFA and the NFA-SiC composites with the sintering temperature at 850–1000 °C. The representative images from the etched NFA sample sintered at 850 °C is shown in Fig. 4. The grains and grain boundaries can be observed in Fig. 4(a). Fig. 4(b) indicates that there are no subgrains involved in the measured grains. It should be noted that the average grain sizes for all the samples are between 6 and 8 μm, although the samples are sintered at different temperatures and with different SiC additives. This means that sintering temperatures and SiC additives do not affect the grain size of the NFA phase to a large extent.

3.3. Density

Fig. 5 shows the relative densities of the pure NFA and NFA-SiC composite samples at different sintering temperatures. The 95 vol% NFA-5 vol% SiC samples have much lower densities than the pure NFA and 97.5 vol% NFA-2.5 vol% SiC samples. The 95 vol% NFA-5 vol% SiC samples have the relative densities of 82 ±1%, 82±2%, 87±2%, 93±3% from 850 °C to 1000 °C, while the 97.5 vol% NFA-2.5 vol% SiC samples have the relative densities of 87 ±1%, 92±1%, 99±1%, 99±2% from 850 °C to 1000 °C, which are close to those of the pure NFA samples, 96±1%, 95±1%, 98±1%, 101±1%, from 850 °C to 1000 °C. All the samples show an increasing tendency for the relative densities with the sintering temperature, which indicates enhanced densification with the temperature. The pure NFA samples have the highest relative densities among the three sintered samples at the same sintering temperature. The increase of the SiC content in the NFA matrix trends to cause less densification of the sintered NFA-SiC composites at the same temperature. Such density changes are consistent with the SEM observations of the porosity for all the samples shown in Fig. 2. Meanwhile, the NFA-SiC composites with 2.5 vol% SiC nearly reach the high densities close to those of the pure NFA samples at the sintering temperatures of 950–1000 °C. However, the relative densities of the NFA-SiC composite with 5 vol% SiC are much lower at the same sintering temperature. This is because the reactions between NFA and SiC become more extensive when more SiC is added. The delay of the densification process for the NFA-SiC composites is reflected from the increasing number of pores indicated by the arrow direction in Fig. 2.

3.4. Mechanical properties

Fig. 6 shows the Vickers hardness of the sintered pure NFA and NFA-SiC composite samples at different sintering temperatures. The hardness of 6–8 GPa for the sintered pure NFA samples is much higher than the reported values of 3–5 GPa [35] and 2.1 GPa [36]. This is attributed to the small average grain size of 6–8 μm. In Fig. 6, the hardness for the NFA-SiC samples is lower than that of the pure NFA samples at 850 °C and 900 °C. With the sintering temperature increase to 950 °C and 1000 °C, the hardness of the NFA-SiC composites exceeds that of the pure NFA samples. Due to the high ductility of the NFA material, the grain boundaries do not play a critical role for the indentation resistance. Thus, there is no relation with the feature of the average grain size shown in Fig. 3. However, the hardness trend shows close correlation with the relative density in Fig. 5. Both the relative density and the hardness increase with the sintering temperature. The lower density samples tend to produce lower hardness.

Another phenomenon is that higher addition of SiC produces lower hardness for the NFA-SiC composites at the same sintering temperature. Thus, the effect of SiC addition on the Vickers hardness is a little complicated for the NFA-SiC composite. This is because during the sintering of the NFA-SiC composites, reactions between NFA and SiC occur as follows: [31–33].

$$SiC \rightarrow Si + C \quad (3)$$

$$Fe + Si \rightarrow FeSi \quad (4)$$

$$Fe + 2Si \rightarrow FeSi_2 \quad (5)$$

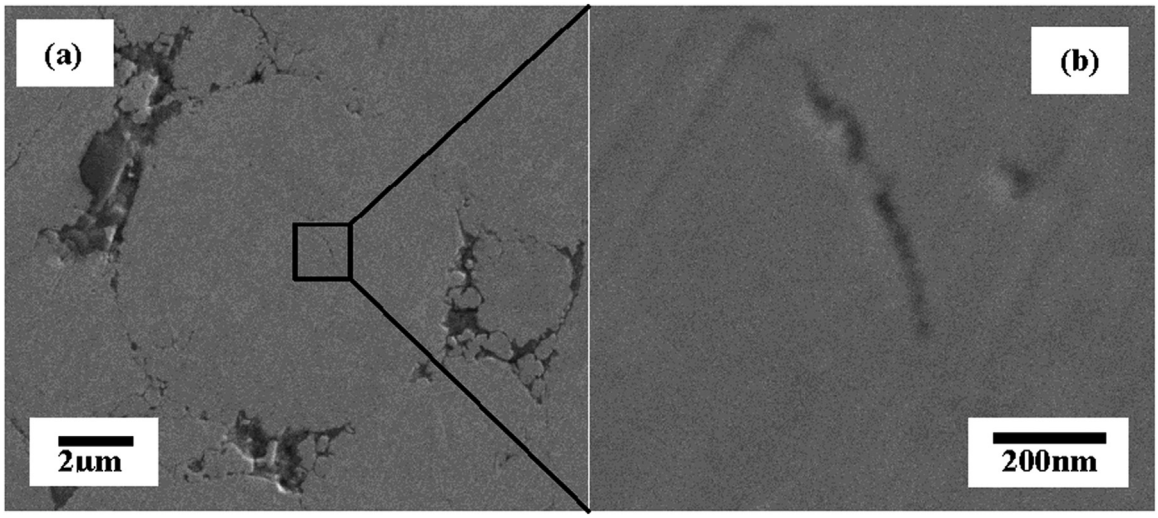

Fig. 4. Representative images of the etched NFA sample sintered at 850 °C.

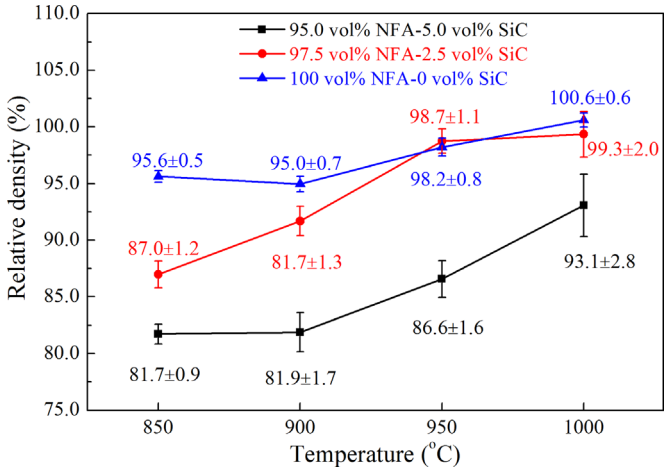

Fig. 5. Relative densities of the NFA and NFA-SiC composite samples at different sintering temperatures.

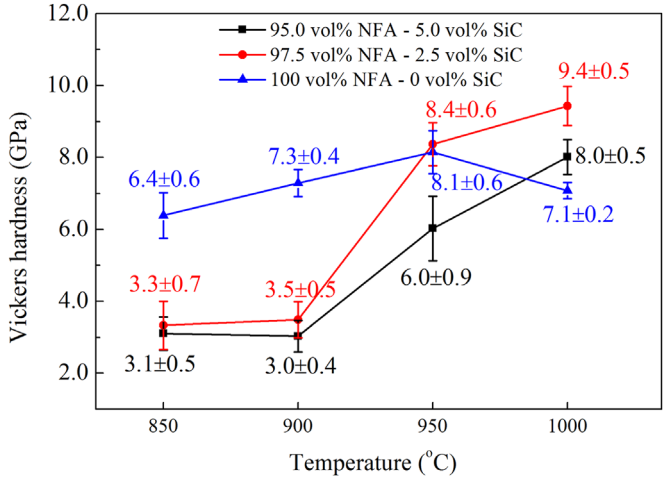

Fig. 6. Vickers hardness of the pure NFA and NFA-SiC composite samples at different sintering temperatures.

$$3Fe + SiC \rightarrow Fe_3Si + 3C \quad (6)$$

$$3Fe + C \rightarrow Fe_3C \quad (7)$$

Even though based on the Si-Fe phase diagram [30], there should be no iron silicide formation due to the low Si content in our system (Si < 3.8 at%), the reaction still occurs. The reason is that Si is not distributed homogeneously in the composites. It has much high content at the interface between NFA and SiC. After sintering, newly formed phases of iron silicides or iron carbide (Fe_3Si, FeSi, $FeSi_2$, and Fe_3C) in the NFA-SiC composite change the microstructures. When more SiC is added, the reactions between NFA and SiC become more intensive, thus producing more low hardness phases. SiC decomposition and newly formed products also lead to a porous structure, which can be seen from the images in Fig. 2(e–h) and (i–l).

The reactions between SiC and Fe are strongly related to the sintering temperature. At the relatively lower temperature range of 850–900 °C, the difference in the hardness between the 2.5 vol% SiC and 5.0 vol% addition samples is small. This is because the positive effect of the sintering temperature plays a more dominant role, and the reaction between NFA and SiC is not intensive. However, when the sintering temperature increases to 950–1000 °C, the hardness of the 5 vol% SiC samples is much lower than that of the 2.5 vol% SiC addition samples. This is because more reaction products are produced due to the high amount of SiC and the intensive reaction between NFA and SiC at the higher sintering temperatures. The effects of the reactions and the sintering temperature on the microstructure of the sintered NFA-SiC composites are also reflected in Fig. 2(e–h) and (i–l). For example, the 97.5 vol% NFA and 95 vol% NFA samples have higher density and lower porosity after 1000 °C sintering than those sintered at 850 °C. Meanwhile, the 97.5 vol% NFA sample at 950 °C sintering temperature has almost the same relative density (99±1%) as that of the pure NFA sample (98±1%), and these two samples also show almost the same hardness value.

It should be noted that there is an initial increase (up to 950 °C) and then a subsequent deterioration (at 1000 °C) in hardness for the pure NFA samples after sintering. The hardness of the sample sintered at 1000 °C has a lower hardness value of 7.1 ± 0.2 GPa. This is believed to be caused by the precipitation of the secondary γ-Fe phase from the α-Fe matrix phase. As shown in Fig. 1, there is

Table 1.
Nano-hardness and the corresponding elemental compositions at local regions for the 97.5 vol% NFA-2.5 vol% SiC sample sintered at 900 °C (the size of each area for EDS measurement is about 3.5 μm×2.7 μm).

Indentation No	Hardness/GPa	Fe/ wt%	Cr/ wt%	C/ wt%	Si/ wt%
1	7.7	83.5	8.6	6.4	1.5
2	12.1	87.0	9.5	3.1	0.4
3	8.3	82.0	10.4	5.6	2.0
4	7.5	83.5	10.1	4.9	1.5
5	11.4	86.8	9.7	3.0	0.5
6	11.8	86.1	9.5	3.2	1.2

a relatively high content of γ-Fe after sintering at 1000 °C. Therefore, the decrease of the hardness is related to the $\alpha \rightarrow \gamma$ iron phase transformation, because γ-Fe has a lower hardness than α-Fe (3.75±0.23 GPa for α-Fe, 3.19±0.16 GPa for γ-Fe [37]). In addition, due to the short sintering time, the newly formed γ-Fe phase cannot be fully densified, which subsequently weakens the microstructure and decreases the hardness of the pure NFA sample further.

To understand the effect of nano-scale local structure on the hardness, an array of nano-indents has been created continuously by automation indentation. Because the size of the nano-indenter tip is only 100 nm, the measurement is very location-specific and the measured values can avoid the effect of pores. The nano-hardness of the 100 vol% NFA, 97.5 vol% NFA-2.5 vol% SiC, and 95 vol% NFA-5 vol% SiC samples after 1000 °C sintering is 8.0 ± 1.7 GPa, 15.9 ± 0.9 GPa, and 14.9 ± 0.7 GPa, respectively. This confirms the changing trend of the Vickers hardness for the samples sintered at 1000 °C. Addition of SiC improves the nano-hardness of the NFA-SiC composites.

The effect of the reaction products on the nano-hardness has also been studied. Nano-hardness values and the corresponding local chemical compositions of different indents for the 97.5 vol% NFA-2.5 vol% SiC sample at 900 °C sintering temperature are presented in Table 1. The indents Nos. 1, 3, and 4 have lower hardness values, while the indents Nos. 2, 5, and 6 show higher nano-hardness values. The regions with higher nano-hardness values contain more Fe, and less C and Si. For example, No. 3 has the nano-hardness of 8.3 GPa with 82.0 wt% Fe, 5.6 wt% C, and 2.0 wt% Si. The regions with lower nano-hardness values contain less Fe, and more C and Si. For example, No. 2 has the nano-hardness of 12.1 GPa with 87.0 wt% Fe, 3.1 wt% C, and 0.4 wt% Si. This means that SiC has diffused into NFA and reacted with NFA, the diffusion

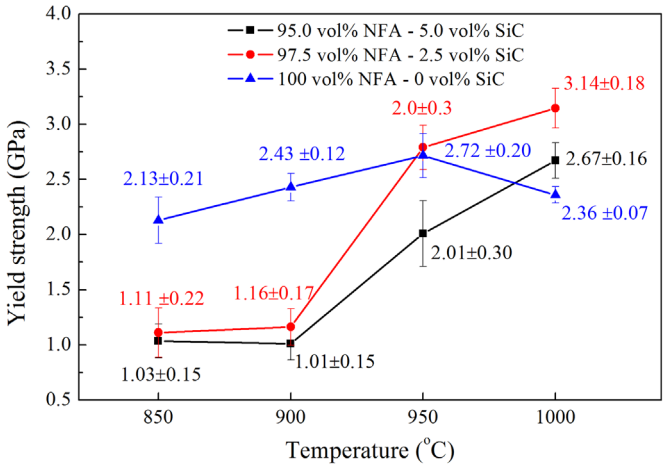

Fig. 7. Yield strength of the pure NFA and NFA-SiC samples at different sintering temperatures.

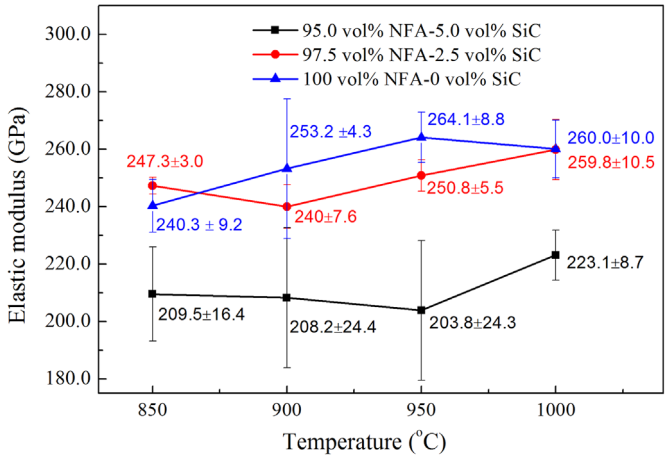

Fig. 8. Elastic modulus of the pure NFA and NFA-SiC samples with different sintering temperatures.

and reaction products lead to lower nano-hardness for the NFA-SiC composites.

The yield strength is obtained as shown in Fig. 7. Because the yield strength is obtained from the Vickers hardness, they show the same trend. In the literature, the yield strength is reported to be 1.45 GPa for 14YWT NFA steel [38], 0.96 GPa for ODS-EUROFER steel [38], and 1.20 GPa for 12Cr-ODS steel [39]. Our pure NFA samples have much higher yield strength of 2.13–2.72 GPa than the reported values. Although the NFA-SiC composites sintered at 850–900 °C show relatively lower yield strength of 1.03–1.16 GPa, they have higher yield strength of 2.01–3.14 GPa when the sintering temperature is increased to 950 °C – 1000 °C. Especially, for the 97.5 vol% NFA-2.5 vol% SiC sample, the yield strength is 2.0 ± 0.3 GPa at 950 °C and 3.14 ± 0.18 GPa at the sintering temperature of 1000 °C, which are much higher than that of the pure NFA samples at the same sintering temperature. This means that the NFA-SiC composite could be a promising high strength composite material for nuclear applications.

The elastic modulus values are obtained along with the nano-hardness during the nano-indentation test and shown in Fig. 8. The 100 vol% NFA sample has the highest elastic modulus, and the 95 vol% NFA-5 vol% SiC sample has the lowest elastic modulus. The addition of SiC decreases the elastic modulus of the composites. This is because the reaction products between NFA and SiC have lower elastic modulus than the pure NFA. Thus, the composite containing more SiC has a lower elastic modulus.

4. Conclusions

In this work, pure NFA samples and SiC-NFA composite samples were prepared using SPS sintering method. Their phase composition, microstructure, density, Vickers hardness, yield tensile strength, nono-hardness, and elastic modulus were investigated. The main conclusions are summarized as follows:

(1) The densification of the NFA and NFA-SiC composites can be enhanced by the sintering temperature, but declined with the SiC addition. The pure NFA and the 97.5 vol% NFA-2.5 vol% SiC samples achieve nearly full density at 950–1000 °C, whereas the 95.0 vol% NFA-5.0 vol% SiC samples have much lower density.

(2) Phase transformation of the pure NFA from α-Fe to γ-Fe happens intensively at the sintering temperature of 1000 °C. However, the phase transformation in the NFA-SiC composites is much less intensive than that in the pure NFA, which means that SiC addition delays γ-Fe formation from α-Fe.

(3) The density and microstructure (phases and reaction

products) are responsible for the mechanical strength of the sintered NFA and NFA-SiC composites. The density is related to the sintering temperature, which has a positive effect on the mechanical strength, while the microstructure is related to the reaction products, which have a negative effect on the mechanical strength. The γ-Fe phase formation in the NFA sintered at 1000 °C causes the decrease in its mechanical strength.

(4) Nano-hardness further demonstrates the lower mechanical strength of the NFA-SiC composites due to the reactions between NFA and SiC.

Acknowledgement

We would like to acknowledge the financial support from Office of Nuclear Energy of Department of Energy under Grant number #DE-NE0008264.

References

[1] L.K. Mansur, A.F. Rowcliffe, R.K. Nanstad, S.J. Zinkle, W.R. Corwin, R.E. Stoller, J. Nucl. Mater. 329 (2004) 166–172.
[2] S.J. Zinkle, J.T. Busby, Mater. Today 12 (2009) 12–19.
[3] S.A. Maloy, M. Toloczko, J. Cole, T.S. Byun, J. Nucl. Mater. 415 (2011) 302–305.
[4] T.S. Byun, J.H. Yoon, S.H. Wee, D.T. Hoelzer, S.A. Maloy, J. Nucl. Mater. 449 (2014) 39–48.
[5] M.J. Alinger, G.R. Odette, D.T. Hoelzer, Acta Mater. 57 (2009) 392–406.
[6] G.R. Odette, M.J. Alinger, B.D. Wirth, Annu. Rev. Mater. Res. 38 (2008) 471–503.
[7] T.S. Byun, J.H. Yoon, D.T. Hoelzer, Y.B. Lee, S.H. Kang, S.A. Maloy, J. Nucl. Mater. 449 (2014) 290–299.
[8] A. Wasilkowska, M. Bartsch, U. Messerschmidt, R. Herzog, A. Czyrska-Filemonowicz, J. Mater. Proc. Technol. 133 (2003) 218–224.
[9] M.B. Toloczko, D.S. Gelles, F.A. Garner, R.J. Kurtz, K. Abe, J. Nucl. Mater. 329 (2004) 352–355.
[10] D.A. McClintock, D.T. Hoelzer, M.A. Sokolov, R.K. Nanstad, J. Nucl. Mater. 386–388 (2009) 307–311.
[11] T.S. Byun, J.H. Kim, J.H. Yoon, D.T. Hoelzer, J. Nucl. Mater. 407 (2010) 78–82.
[12] Y. Katoh, K. Ozawa, C. Shih, T. Nozawa, R.J. Shinavski, A. Hasegawa, L.L. Snead, J. Nucl. Mater. 448 (2014) 448–476.
[13] L.L. Snead, T. Nozawa, M. Ferraris, Y. Katoh, R. Shinavski, M. Sawan, J. Nucl. Mater. 417 (2011) 330–339.
[14] L. Giancarli, H. Golfier, S. Nishio, R. Raffray, C. Wong, R. Yamada, Fusion Eng. Des. 61–62 (2002) 307–318.
[15] Y. Katoh, L.L. Snead, I. Szlufarska, W.J. Weber, Curr. Opin. Solid State Mater. Sci. 16 (2012) 143–152.
[16] R. Naslain, Compos. Sci. Technol. 64 (2004) 155–170.
[17] N.B. Morley, Y. Katoh, S. Malang, B.A. Pint, A.R. Raffray, S. Sharafat, S. Smolentsev, G.E. Youngblood, Fusion Eng. Des. 83 (2008) 920–927.
[18] A.R. Raffray, R. Jones, G. Aiello, M. Billone, L. Giancarli, H. Golfier, A. Hasegawa, Y. Katoh, A. Kohyama, S. Nishio, B. Riccardi, M.S. Tillack, Fusion Eng. Des. 55 (2001) 55–95.
[19] L. Charpentier, K. Dawi, M. Balat-Pichelin, E. Beche, F. Audubert, Corros. Sci. 59 (2012) 127–135.
[20] F. Guillard, A. Allemand, J.D. Lulewicz, J. Galy, J. Eur. Ceram. Soc. 27 (2007) 2725–2728.
[21] H. Tanaka, J. Ceram. Soc. Jpn. 119 (2011) 218–233.
[22] C. Menapace, I. Lonardelli, M. Tait, A. Molinari, Mat. Sci. Eng. A – Struct. 517 (2009) 1–7.
[23] S. Pasebani, I. Charit, J. Alloy Compd. 599 (2014) 206–211.
[24] K. Serivalsatit, B. Kokuoz, B. Yazgan-Kokuoz, M. Kennedy, J. Ballato, J. Am. Ceram. Soc. 93 (2010) 1320–1325.
[25] K.J. Ning, J. Wang, D.W. Luo, J. Ma, J. Zhang, Z.L. Dong, L.B. Kong, D.Y. Tang, Opt. Mater. 50 (2015) 21–24.
[26] I. Brooks, P. Lin, G. Palumbo, G.D. Hibbard, U. Erb, Mat. Sci. Eng. A 491 (2008) 412–419.
[27] F. Khodabakhshi, M. Haghshenas, H. Eskandari, B. Koohbor, Mat. Sci. Eng. A 636 (2015) 331–339.
[28] I.A. Yakubtsov, P. Poruks, J.D. Boyd, Mat. Sci. Eng. A 480 (2008) 109–116.
[29] J.H. Yoon, Y. Lee, S.H. Kang, T.S. Byun, D.T. Hoelzer, Curr. Nanosci. 10 (2014) 47–50.
[30] J. Lacaze, B. Sundman, Met. Trans. A 22 (1991) 2211–2223.
[31] J. Li, B.Y. Zong, Y.M. Wang, W.B. Zhuang, Mat. Sci. Eng. A 527 (2010) 7545–7551.
[32] J. Pelleg, Mat. Sci. Eng. A 269 (1999) 225–241.
[33] T.D. Shen, C.C. Koch, K.Y. Wang, M.X. Quan, J.T. Wang, J. Mater. Sci. 32 (1997) 3835–3839.
[34] A. Bedolla-Jacuinde, W. Rainforth, I. Mejia, Met. Mater. Trans. A 44A (2013) 856–872.
[35] S. Kobayashi, K. Nakai, Y. Ohmori, Acta Mater. 49 (2001) 1891–1902.
[36] S. Kikuchi, Y. Nakahara, J. Komotori, Int. J. Fatigue 32 (2010) 403–410.
[37] K.R. Gadelrab, G. Li, M. Chiesa, T. Souier, J. Mater. Res. 27 (2012) 1573–1579.
[38] D.A. McClintock, M.A. Sokolov, D.T. Hoelzer, R.K. Nanstad, J. Nucl. Mater. 392 (2009) 353–359.
[39] A. Chauhan, D. Litvinov, J. Aktaa, J. Nucl. Mater. 468 (2016) 1–8.